Hybrid Finite Element-Finite Volume Algorithm for Solving Transient Multi-Scale Non-Linear Fluid-Structure Interaction during Operation of a Hydraulic Seal

Azam Thatte[*, 1], Richard F. Salant [1]
[1]Georgia Institute of Technology
*Corresponding author: MRDC, Room 4111, Georgia Institute of Technology, Atlanta, GA 30332-0405
azamthatte@gatech.edu

Abstract: This paper presents a hybrid finite element – finite volume algorithm for solving multi-scale fluid-structure interaction during transient operation of a hydraulic rod seal. The elasto-hydrodynamic model consists of analyses of the macro-scale structural mechanics of the seal deformations, a macro-scale elastic contact mechanics at the seal-rod interface, the micro-scale fluid mechanics of the lubricating film in the sealing zone, the micro-scale statistical contact mechanics of the contacting asperities on the seal lip and the micro-scale elastic deformation mechanics of the sealing zone, all incorporated in a single hybrid iterative computational framework to solve these highly coupled nonlinear multiphysics equations simultaneously. Finite element calculations using COMSOL's PDE and Structural Mechanics modules are coupled with finite volume calculations in MATLAB to form a hybrid MATLAB based framework. The hybrid method facilitates an online calculation of micro-scale deformations necessary to model the transient seal response. Results for axial deformations, principal stress distribution in the seal body and net leakage along with cyclic histories of film thickness, fluid pressure and contact pressure distributions are presented which reveal some key characteristics of transient seal performance.

Keywords: Fluid-Structure, Multiscale, Hybrid, FEA, Contact

1. Introduction

The reciprocating rod seal is one of the most critical elements in a hydraulic system since it is relied on to prevent leakage of hydraulic fluid into the surroundings. It is fitted to the rod with an interference fit and lubricant, in the form of the sealed hydraulic fluid is present in the interface between the seal and the rod in order to prevent excessive wear & frictional losses and high temperatures.

During outstroke, fluid is dragged out of the cylinder by adhering to the moving rod. During the instroke, it is dragged back into the cylinder. For zero net leakage per cycle, the fluid transport during the outstroke must be less than the potential fluid transport during the instroke.

Although important experimental and theoretical studies have been performed in the past, it is only recently that numerical modeling has revealed some of the significant fundamental physical phenomena that govern the behavior of such seals [1]-[5]. Prior steady state numerical models of reciprocating hydraulic rod seals [3]-[5] have used offline finite element codes to predict the micron scale deformations of a seal under the combined action of contact pressure and fluid pressure in the sealing zone (influence coefficient method). In turn, they use these deformations for solving Reynolds equation for the fluid pressure in the seal-rod interface, iteratively. The limitation of such an offline approach is that it cannot be used efficiently to predict seal deformations during transient operation. Due to the changing sealed pressure, the seal would assume a time-varying geometrical configuration and influence coefficients would have to be calculated at every time step, which is an inefficient process. As a first step to remedy this problem, in the present study, a hybrid finite element – finite volume transient algorithm has been developed to take account of the time varying rod velocity. In this approach, the solution does not require influence coefficients to be calculated beforehand and the micro-scale deformations are calculated at each time step during solution process itself.

2. Model and Analysis

Figure 1 shows a schematic of a typical reciprocating hydraulic rod seal. The region where the seal lip appears to meet the rod is termed the sealing zone and is shown on the

right side. Since the rod is much smoother than the seal lip due to polishing during the run-in period, the rod is treated as perfectly smooth while the seal lip is treated as rough. The elasto-hydrodynamic model consists of analyses of the macro-scale structural mechanics of the seal deformations, the macro-scale elastic contact mechanics at the seal-rod interface, the micro-scale fluid mechanics of the lubricating film in the sealing zone, the micro-scale statistical contact mechanics of the contacting asperities on the seal lip and the micro-scale elastic deformation mechanics of the sealing zone, all incorporated in a single hybrid iterative computational framework to solve these highly coupled nonlinear multiphysics equations simultaneously.

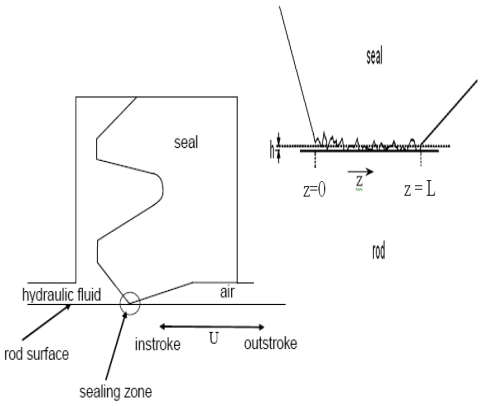

left: seal system. right: blown up sealing zone
Figure 1. Schematic of Rod Seal

2.1 Macro-Scale Deformation Mechanics

The macro-scale deformation mechanics for the seal mounted between the housing and rod, under pressurized conditions, is solved using an in-house MATLAB code coupled with the COMSOL's finite element code. The seal is modeled as a nearly incompressible, linear, elastic and isotropic material with small deformation theory**.** The finite element mesh consists of 11494 2nd order Lagrange elements (based on a mesh refinement study). The principle of virtual work for the axisymmetric system reads,

$$2\pi\int_A\left(-\boldsymbol{\sigma}^T\boldsymbol{\varepsilon}(\mathbf{u}_{test})+\mathbf{u}_{test}^T\mathbf{F}_V\right)rdA + 2\pi\int_l\mathbf{u}_{test}^T\mathbf{F}_l\,r\,dl+\sum_i\mathbf{u}_{test}^T\mathbf{F}_i=0 \quad (1)$$

Eq.(1) when written in terms of stress and strain components becomes,

$$2\pi\int_A r\begin{pmatrix}-\varepsilon_{r\,test}\sigma_r-\varepsilon_{\theta\,test}\sigma_\theta-\varepsilon_{z\,test}\sigma_z\\-2\varepsilon_{rz\,test}\tau_{rz}+r.uor_{test}F_r+w_{test}F_z\end{pmatrix}dA + 2\pi\int_l r\left(r.uor_{test}F_r+w_{test}F_z\right)dl + \left(r.uor_{test}F_r+w_{test}F_z\right)=0 \quad (2)$$

To model near incompressibility, a mixed formulation is used whereby the negative mean stress, $\tilde{p}$, is added as a new dependent variable. The stress tensor $\boldsymbol{\sigma}$ is then decomposed into a deviatoric part, $\boldsymbol{\sigma}_d$ and a mean part, $-\tilde{p}$ such that the equation for $\tilde{p}$ in terms of the strain tensor is given as,

$$\tilde{p}=\tilde{p}_0-K\,\mathbf{m}^T\left(\boldsymbol{\varepsilon}-\boldsymbol{\varepsilon}_0\right) \quad (3)$$

where $\mathbf{m}=[1\,1\,0\,1]^T$.

The macro-scale deformation mechanics and the macro-scale contact mechanics analysis (described in sections (2.4) & (2.5) respectively) yield the deformed geometrical configuration, contact zone and the dry contact pressure distribution at the interface between the seal and the rod, all of which serve as input for the micro-scale fluid-structure interaction model at each time step.

2.2 Micro-Scale Fluid Mechanics

The micro-scale fluid mechanics in the sealing zone is governed by the transient Reynolds equation. Noting that the seal is axisymmetric and the film thickness is very small compared to the seal radius, the flow is modeled as one-dimensional. Since cavitation may occur and squeeze film effects can be significant, the following form of the Reynolds equation is used.

$$\frac{\partial}{\partial\hat{z}}\left(\phi_{xx}H^3e^{-\hat{\alpha}F\phi}\frac{\partial}{\partial\hat{z}}(F\phi)\right)= 6\zeta\frac{\partial}{\partial\hat{z}}\left(\{1+(1-F)\phi\}\{H_T+\phi_{s.c.x}\}\right)+12\varepsilon\frac{\partial}{\partial\hat{t}}\left(\{1+(1-F)\phi\}H_T\right) \quad (4)$$

The flow factors ϕ_{xx} and $\phi_{s.c.x}$ account for the surface roughness effects of the seal lip.

In the liquid region,

$$\phi \geq 0,\ F=1 \text{ and } P=\phi \tag{5}$$

In the cavitated region,

$$\phi<0,\ F=0,\ P=0 \text{ and } \hat{\rho}=1+\phi \tag{6}$$

The boundary conditions are,

$$\begin{aligned} P &= P_{sealed} \text{ at } \hat{z}=0 \\ P &= 1 \quad \text{at } \hat{z}=1 \end{aligned} \tag{7}$$

The average truncated film thickness is given by,

$$H_T = \int_{-H}^{\infty} (H+\delta) f(\delta) d\delta \tag{8}$$

In the model, a Gaussian distribution for film thickness is assumed, yielding,

$$H_T = \frac{H}{2} + \frac{H}{2} erf\left[\frac{H}{\sqrt{2}}\right] + \frac{1}{\sqrt{2\pi}} e^{-H^2/2} \tag{9}$$

Equations (4)-(6) along with boundary condition eq. (7) are solved for ϕ and F at each time step numerically with a finite volume formulation. The finite volume mesh consists of 236 nodes (selected following a mesh sensitivity study). The resulting set of linear algebraic equations is solved using the tri-diagonal matrix algorithm (TDMA). Time integration is carried out using a fully implicit method giving an unconditional numerical stability to the procedure. This yields the fluid pressure distribution and location of cavitation zones at each time step.

2.3 Micro-Scale Contact Mechanics

Since significant asperity contact may occur (mixed lubrication), it is necessary to add an asperity contact pressure to the hydrodynamic pressure in computing the normal seal deformation and local film thickness. Assuming a Gaussian distribution of asperity heights, the micro-scale contact pressure is given by,

$$P_c = \frac{4}{3} \frac{1}{\left(1-\nu^2\right)} \hat{\sigma}^{3/2} \frac{1}{\sqrt{2\pi}} \int_{H}^{\infty} (\delta - H)^{3/2} e^{-\delta^2/2} d\delta \tag{10}$$

The integral in eq. (10) is evaluated numerically using the Adaptive Gauss-Kronrod quadrature.

2.4 Micro-Scale Deformation Mechanics

To compute the micro-scale film thickness distribution at each time step, it is necessary to compute the radial deformation of the sealing element under the combined action of the sealed pressure, the fluid pressure in the sealing zone and the contact pressure at that time step. Having obtained the fluid pressure distribution from the solution of eq. (4) and the contact pressure distribution from eq. (10), a net pressure load of $\left(P_t - P_{dc}\right)$ is applied over the contact length, and the corresponding radial deformations $\left(H_{def}\right)_i$ of the sealing zone edge are obtained from the micro-scale finite element calculations using the approach of section (2.1). Here P_t is the sum of the fluid pressure and micro-scale contact pressure. In discretized form with n axial nodes along the sealing zone, the film thickness at the i^{th} node can be expressed as,

$$H_i = H_d + \left(H_{def}\right)_i \tag{11}$$

where the dry film thickness, H_d, is the thickness that a hypothetical film would occupy under dry contact conditions (in the absence of fluid in the sealing zone). It is computed by equating the dry contact pressure obtained from the macro-scale finite element analysis of the smooth seal surface under pressurized conditions, P_{dc}, with the contact pressure distribution computed from eq. (10) under dry conditions. Using a curve fit method to invert eq. (10) yields,

$$\begin{aligned} H_d &= a + b \cdot \log(x) + c \cdot (\log(x))^2 \\ &+ d \cdot (\log(x))^3 + e \cdot (\log(x))^4 + f \cdot (\log(x))^5 \end{aligned} \tag{12}$$

where $x = -\log_{10}|I|$, $I = \dfrac{P_{dc}}{\frac{4}{3}\frac{1}{\left(1-\nu^2\right)}\hat{\sigma}^{3/2}}$

and a = 0.86197, b = 1.16979, c = 0.34673, d = 3.57134, e = 1.07985, f = 1.68629.

2.5 Macro-Scale Contact Mechanics

To obtain P_{dc} above, the macro-scale finite element contact mechanics at the seal-rod interface and seal-housing interface is handled using the augmented Lagrangian method. These

calculations form an integral part of the macro-scale deformation mechanics described in section (2.1). Here, an augmentation component is introduced for the dry contact pressure P_{dc} . For each slave point at location X of interest a corresponding master point $\Re(X)$ is searched in the direction perpendicular to the slave boundary. As the boundaries approach each other, the master point converges to the closest point as the gap goes to zero. The contact interaction gives the following contribution to the weak form on the slave boundary,

$$\int_{slave}\left[\begin{array}{r}\left(P_{dc,p}\delta\lambda+P_{dt,p}\cdot\Re(\mathbf{F}_D)\delta(\Re(X))\right)\\+\left(C_1\delta P_{dc}+C_2\cdot\delta P_{dt}\right)\end{array}\right]dA$$

Where the contact variable C_1 depends on the difference between the penalized dry contact pressure values at the previous and current augmented solver iterations while the contact variable C_2 depends on the difference between the previous and current penalized dry traction values. The augmented dry contact pressure $P_{dc,p}$ defined on the slave boundary is given by [6],

$$P_{dc,p}=P_{dc}-\varepsilon_n\lambda \quad ;\ \lambda\le 0 \qquad (13\text{ a})$$

Here ε_n is the normal penalty factor and λ is the gap between the slave and master boundaries. When the boundaries are not yet in contact ($\lambda>0$), a pressure that increases rapidly as the master approaches the slave is given as,

$$P_{dc,p}=P_{dc}\ \exp\left(-\frac{\varepsilon_n\ \lambda}{P_{dc}}\right);\ \ \lambda>0 \qquad (13b)$$

The penalized dry friction traction $P_{dt,p}$ is defined on the slave boundary as,

$$P_{dt,p}=P_{dt,test}\frac{P_{dt,cr}}{\left|P_{dt,test}\right|} \qquad (14)$$

where

$$P_{dt,test}=P_{dt}-\varepsilon_t\,\Re(\mathbf{F}_D)\left(\Re(X)-\Re(X)_{old}\right)$$

$$P_{dt,cr}=R_c+f\,P_{dc,p}$$

and $\Re(\mathbf{F}_D)\left(\Re(X)-\Re(X)_{old}\right)$ is the axial slip that occured since the previous time step.

3. Algorithm

COMSOL's ability to be run from within the MATLAB environment and to export the FEM structure to MATLAB is utilized to form a coupled, finite element – finite volume framework to solve this multiphysics problem.

Step a) Initially, the macro-scale deformation & dry contact mechanics is solved using COMSOL's structural mechanics module to yield the contact zone and the dry contact pressure distribution under the application of the sealed pressure. The corresponding contact zone length and dry contact pressure variables are stored in an FEM structure, which is exported to the parent MATLAB script.

Step b) Equations (4)-(6) along with boundary condition eq. (7) are then solved for ϕ and F at each time step numerically with a finite volume formulation and TDMA algorithm using a MATLAB script. This yields the fluid pressure distribution and locations of cavitation zones.

Step c) The micro-scale asperity contact pressure is then evaluated using the Greenwood-Williamson statistical model (eq. (10)).

Step d) The micro-scale fluid and asperity contact pressures along with the macro-scale dry contact pressure calculated earlier are then fed into the micro-scale finite element seal deformation analysis to calculate the micro-scale radial deformations $\left(H_{def}\right)_i$ of the sealing edge.

This finite element calculation is performed using COMSOL structural mechanics script called within the parent MATLAB script. The computed deformations are then used to update the film thickness for the next iteration using eq. (11).

Step e) Steps (b) through (d) are run in an iterative loop in a coupled finite element – finite volume framework within the parent MATLAB script until the converged solutions for fluid pressure and film thickness are obtained at that particular time step.

This gives the solution of the coupled problem at the first time step.

Step f) The converged solutions at the first time step are then used to calculate the transient

squeeze term (in eq. (4)) for the next time step (in TDMA part of finite-volume algorithm).

Step g) The transient solution for the entire period of operation is obtained by updating the initial guess with the previous time step solution and repeating steps (b) through (f) over the entire outstroke-instroke time period of seal operation.

4. Post-Processing Calculations

After arriving at the solution for the entire time period of interest, auxiliary calculations are performed for quantities such as fluid transport rate and total fluid transport. Having stored the solution history, the instantaneous transport rate (flow rate per unit circumferential length through the film) and the amount of transport (over elapsed time T_i) can be found respectively from,

$$\hat{q} = -\phi_{xx} H^3 e^{-\hat{\alpha} F\phi} \frac{\partial(F\phi)}{\partial \hat{z}} + 6\zeta\left(\{1+(1-F)\phi\}\{H_T+\phi_{s.c.x}\}\right) \quad (15)$$

$$\hat{Q} = \int_0^{T_i} \hat{q}\, d\hat{t} \quad (16)$$

5. Results

Computations have been performed for the typical seal shown in figure 2a (black lines) with base parameters of: E = 43 x 10^6 Pa, υ = 0.49, μ_0 = 0.043 Pas, α = 20 x 10^{-9} Pa^{-1}, R = 1.0 µm, η = 10^{12} m^{-2}, f = 0.25, rod diameter = 88.9 mm, stroke length = 1.93 m, seal width = 6.8 mm, $t_{reference}$ = 1 sec. The seal roughness is assumed to be isotropic. As described earlier, the rod is treated as perfectly smooth. The sealed pressure is held constant at p_{sealed} = 6.9 MPa (1000 psi) and only the rod speed varies with time. All of the following results are for a seal roughness of 1.1 microns, which will be shown to be a non-leaking seal.

Figure 2 shows the mounted and pressurized seal, a result obtained after macro-scale deformation & contact mechanics calculations. Figure 2a shows the macroscopic axial displacements of the seal body varying from 0 mm (blue) to 0.5 mm (red). Zero axial displacements on the back side of the seal are due to the axial mechanical constrains placed there. Black lines show the geometry before application of the sealed pressure. Figure 2b shows the deformed mesh configuration and the sealing zone obtained after these calculations. They serve as inputs for the micro-scale deformation mechanics model. Figure 2c shows the first principal stress contours in the seal body. Contours converge in the key areas showing stress concentrations. The stress contour distribution is expected to play a key role in calculating microscopic deformations of the sealing edge. Figure 2d shows the dry contact pressure distribution over the sealing zone.

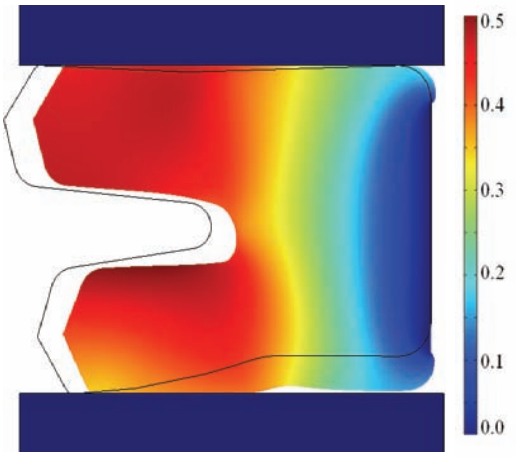

2a: Axial Displacements (mm)

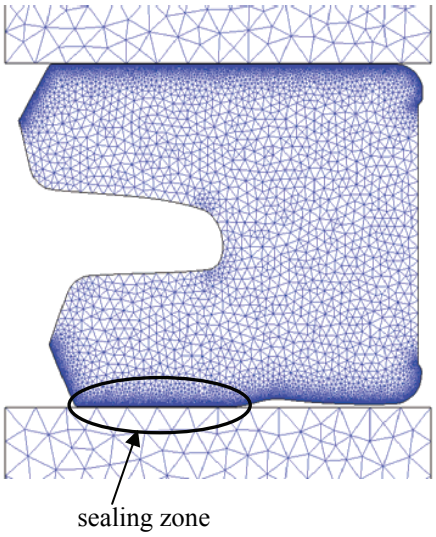

2b: Deformed Mesh & Sealing Zone after macro-scale contact mechanics.

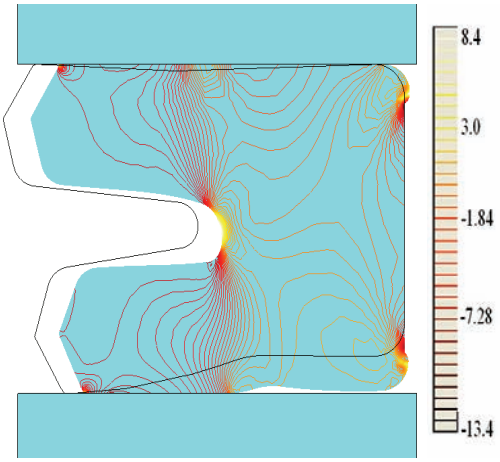

2c: First Principal Stress in the Seal Body

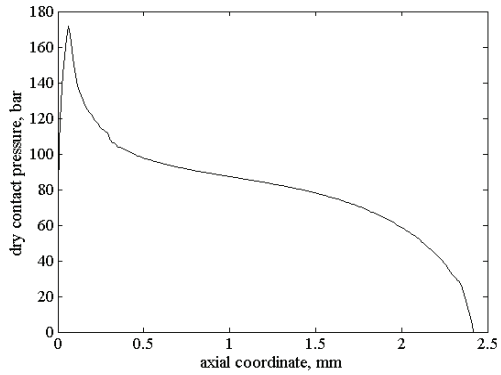

2d: Dry Contact Pressure Distribution over the Sealing Zone

Figure 2. Macro-Scale Deformation Mechanics Results.

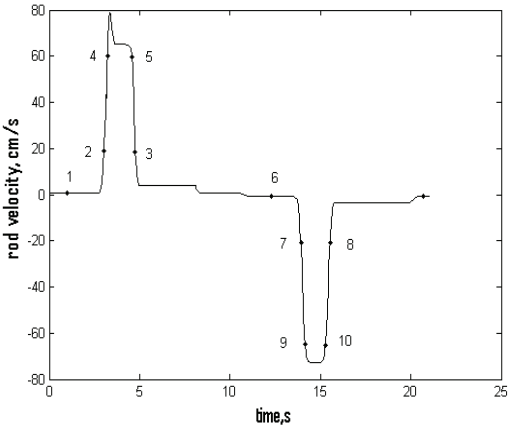

Figure 3. Rod Velocity vs. Time

Figure 3 shows the rod velocity as a function of time, over one cycle. The outstroke occurs from t = 0 to t = *10.50* sec., and the instroke from t = 10.51 sec. to t = 21.0 sec. Also shown on this figure are key times labeled 1 to 10.

The film thickness, fluid pressure and contact pressure distributions during outstroke and instroke for the key points (from figure 3) are shown in figures 4-6. The legends in these figures show the key points from figure 3. In figures 4 through 6, curves for points 4 & 5 overlap. Same is true for points 9 & 10.

From figure 4 it is seen that mixed lubrication occurs, since the film thickness is generally less than 3σ. During the outstroke, as the rod speed increases, the film thickness decreases; during the instroke the opposite occurs, as the rod speed increases, the film thickness increases. Thus the film is always thicker during the instroke than during the outstroke, which has been shown to be favorable for preventing leakage [3].

Figure 5 shows that during the outstroke the fluid pressures decrease with increasing rod speed, while during the instroke they increase with increasing rod speed, explaining the film thickness behavior. This is because during the outstroke the flow is predominantly diverging, and during the instroke it is primarily converging. During the outstroke the fluid cavitates (flat zero pressure region), which has also been shown to be favorable for preventing leakage [3]. The differences in pressures between points 2 and 3, and between points 7 and 8, illustrate the squeeze film effect.

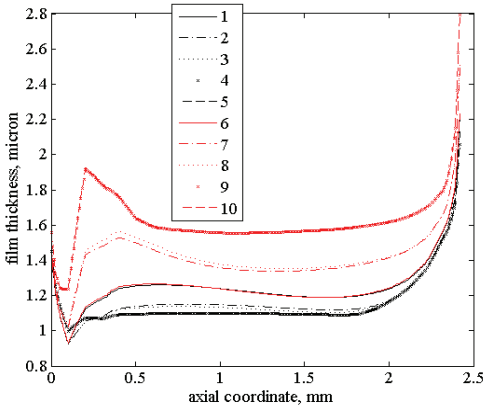

Figure 4. Film Thickness Distribution during Outstroke (black) & Instroke (red)

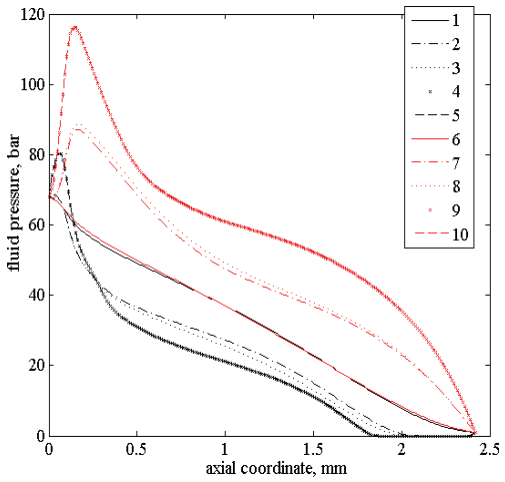

Figure 5. Fluid Pressure Distribution during Outstroke (black) & Instroke (red)

The contact pressure distributions in figure 6 show that the contact pressures increase with increasing rod speed during the outstroke, and decrease with increasing rod speed during the instroke. This is consistent with both the film thickness distributions and the fluid pressure distributions.

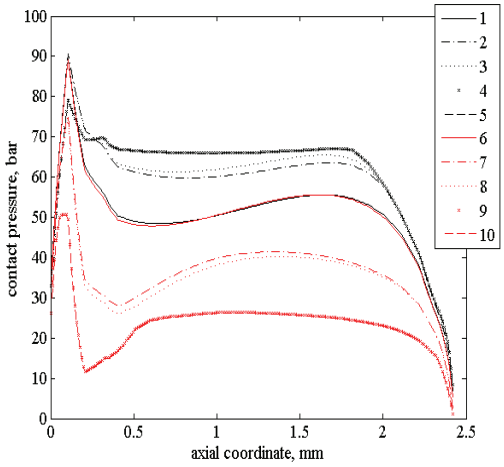

Figure 6. Contact Pressure Distribution during Outstroke (black) & Instroke (red)

Figure 7 shows the net fluid transport out of the cylinder as a function of time. During the outstroke it increases and during the instroke it decreases. At the end of the cycle (t = 21.0 sec.) it has a negative value, indicating zero net leakage.

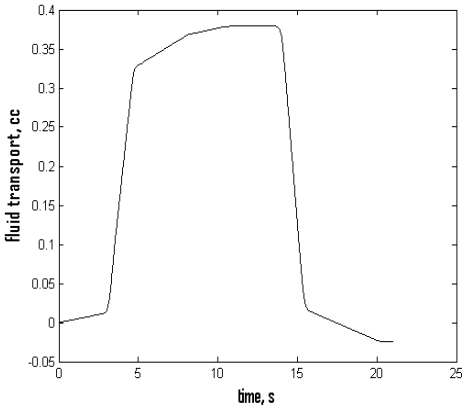

Figure 7. Fluid Transport vs. Time

6. Conclusions

A hybrid framework of finite element – finite volume solution algorithm for solving highly coupled, nonlinear, multiscale fluid-structure interaction equations is presented. The new hybrid method facilitated an *In-Situ* calculation of micro-scale deformations necessary to model the transient seal respose. The transient elastohydrodynamics solution obtained revealed the history of a reciprocating seal's behavior over a cycle. It showed that thinner films during the outstroke than during the instroke, and cavitation during the outstroke, are characteristics of non-leaking seals. It also provided insight into why the behaviors during outstroke and instroke differ.

7. Nomenclature

E	elastic modulus
F	cavitation index
f	friction coefficient
$\mathbf{F}_v$	volumetric body force vector
$\mathbf{F}_l$	surface traction vector
$\mathbf{F}_i$	point load vector
$\mathbf{F}_D$	deformation gradient tensor
H	dimensionless average film thickness, h/σ

H_T dimensionless average truncated film thickness, h_T/σ

K bulk modulus for seal material

L length of solution domain in z direction

P dimensionless fluid pressure, p / p_a

p_a ambient pressure

P_c dimensionless contact pressure for deformation analysis, p_c / E

P_{dc} dimensionless dry contact pressure, p_{dc} / E

P_{sealed} dimensionless sealed pressured, p_{sealed} / p_a

$\tilde{p}_0$ negative mean of initial stress vector $\boldsymbol{\sigma}_0$

$\hat{q}$ dimensionless flow rate per unit circumferential length, $12\mu_0 qL/(p_a\sigma^3)$

r radial coordinate

R asperity radius

R_c cohesion sliding resistance

$\hat{t}$ dimensionless time, $t / t_{reference}$

U surface speed of rod

$\mathbf{u}_{test}$ displacement test function vector for virtual work

uor variable used to avoid division by r, u/r

u radial displacement

w axial displacement

$\hat{z}$ dimensionless axial coordinate, z / L

$\hat{\alpha}$ dimensionless pressure-viscosity coefficient, αp_a

$\hat{\varepsilon}$ $\mu_0 L^2/(\sigma^2 p_a t_{reference})$

$\boldsymbol{\varepsilon}_0$ initial strain vector

ϕ fluid pressure/density function

$\phi_f, \phi_{fss}, \phi_{fpp}$ shear stress factors

$\phi_{s.c.x}$ shear flow factor

ϕ_{xx} pressure flow factor

μ_0 viscosity at atmospheric pressure

$\hat{\rho}$ dimensionless density,

ρ_l liquid density

$\Re$ contact map operator

$\hat{\sigma}$ dimensionless rms roughness of sealing element surface, $\sigma R^{1/3}\eta^{2/3}$

$\boldsymbol{\sigma}_0$ initial stress vector

υ Poisson's ratio

ξ $R^{1/3}\eta^{2/3} E L / p_a$

ς dimensionless rod speed, $\mu_0 UL/(\sigma^2 p_a)$

η asperity density

8. References

1. Nikas, G. K., "Elastohydrodynamics and Mechanics of Rectangular Elastomeric Seals for Reciprocating Piston Rods," J. of Tribology, **125**, pp. 60-69 (2003).

2. Nikas, G. K, "Transient Elastohydrodynamic Lubrication of Rectangular Elastomeric Seals for Linear Hydraulic Actuators," J. of Engineering Tribology, **217**, pp. 461-473 (2003).

3. Salant, R. F., Maser, N. and Yang, B., "Numerical Model of a Reciprocating Hydraulic Rod Seal," Journal of Tribology, **129**, pp. 91-97 (2007).

4. Yang, B. and Salant, R. F., "Numerical Model of a Reciprocating Hydraulic Rod Seal with a Secondary Lip," Tribology Transactions, **51,** pp. 119-127 (2008).

5. Yang, B. and Salant, R. F., "Numerical Model of a Tandem Reciprocating Hydraulic Rod Seal," Journal of Tribology, **130,** pp. 032201-1 – 032201-7 (2008).

6. Pietrzak, G. and Curnier, A., "Large deformation frictional contact mechanics: continuum formulation and augmented Lagrangian treatment," Comput. Methods Appl. Mech. Engrg. **177,** pp. 351-381 (1999).

9. Acknowledgements

The authors gratefully acknowledge the Georgia Power Company and the National Science Foundation, Engineering Research Center for Compact and Efficient Fluid Power for their support.